

# An Optomechanical Model Eye for Ophthalmological Refractive Studies

Ashkan Arianpour; Eric J. Tremblay, PhD; Igor Stamenov; Joseph E. Ford, PhD;  
David J. Schanzlin, MD; Yuhwa Lo, PhD

## ABSTRACT

**PURPOSE:** To create an accurate, low-cost optomechanical model eye for investigation of refractive errors in clinical and basic research studies.

**METHODS:** An optomechanical fluid-filled eye model with dimensions consistent with the human eye was designed and fabricated. Optical simulations were performed on the optomechanical eye model, and the quantified resolution and refractive errors were compared with the widely used Navarro eye model using the ray-tracing software ZEMAX (Radiant Zemax, Redmond, WA). The resolution of the physical optomechanical eye model was then quantified with a complementary metal-oxide semiconductor imager using the image resolution software SFR Plus (Imatest, Boulder, CO). Refractive, manufacturing, and assembling errors were also assessed. A refractive intraocular lens (IOL) and a diffractive IOL were added to the optomechanical eye model for tests and analyses of a 1951 U.S. Air Force target chart.

**RESULTS:** Resolution and aberrations of the optomechanical eye model and the Navarro eye model were qualitatively similar in ZEMAX simulations. Experimental testing found that the optomechanical eye model reproduced properties pertinent to human eyes, including resolution better than 20/20 visual acuity and a decrease in resolution as the field of view increased in size. The IOLs were also integrated into the optomechanical eye model to image objects at distances of 15, 10, and 3 feet, and they indicated a resolution of 22.8 cycles per degree at 15 feet.

**CONCLUSIONS:** A life-sized optomechanical eye model with the flexibility to be patient-specific was designed and constructed. The model had the resolution of a healthy human eye and recreated normal refractive errors. This model may be useful in the evaluation of IOLs for cataract surgery.

[J Refract Surg 2013;29:XX-XX.]

**S**ynthetic optical components that match the sophistication and features of a crystalline lens are difficult to construct, although the need for corrective intraocular lenses (IOLs) after cataract surgery is pressing. The development cycle of IOLs is lengthy and the process costly, especially because of the requisite testing on primates, which have accommodation mechanisms comparable to those of humans.<sup>1</sup> Moreover, assessment of the quality of vision over the range of accommodation is lacking in animal studies. Finally, a significant number of claims made by patients after surgery about poor visual acuity are related to incorrect measurements of patient biometry and the selection of IOLs.<sup>2</sup>

A life-sized eye model capable of evaluating vision restoration after crystalline lens replacement with an IOL would be of great value in both ophthalmology research and eye clinics and would be a welcome addition to current biometric technologies.<sup>3,4</sup> Such a device would allow ophthalmologists to analyze optical images unprocessed by the brain. The device could aid the design and research of the IOL or contact lens because characterizing a single lens component by experiment or simulation cannot produce the same amount of relevant information as characterizing the lens within a complete, real-size eye model.

Before our work, other efforts had been made to fabricate eye models to recreate images with crystalline lenses or IOLs<sup>5-11</sup> for assessment of the quality of soft contact lenses.<sup>12</sup> Most of these eye models use glass or polymer lenses to either directly couple the images to a complementary metal-oxide semiconductor (CMOS) sensor or transfer the images to the CMOS

*From the Jacobs School of Engineering (AA, EJT, IS, JEF, YL) and the Department of Ophthalmology (DJS), University of California–San Diego, La Jolla, California.*

*Submitted: August 5, 2012; Accepted: November 20, 2012*

*Supported by 25677A-DARPA/HR0011-10-1-005.*

*The authors have no financial or proprietary interest in the materials presented herein.*

*The authors thank Scripps Institute of Oceanography for manufacturing the optomechanical design.*

*Correspondence: Ashkan Arianpour, 9500 Gilman Drive, Mail Code 0407, La Jolla, CA 92093. E-mail: ash.arianpour@gmail.com*

TABLE 1  
**Specifications of Navarro Eye Model and Current Optomechanical Eye Model**

No.	Notation	Radius (mm)	Thickness (mm)	Index $n$	Aspheric $k$
Navarro eye model					
1	Cornea	7.72	0.55	1.367	-0.260
2	Anterior chamber	6.50	3.05	1.337	0
3	Crystalline lens	10.20	4.00	1.420	-3.136
4	Vitreous humor	-6.00	16.40	1.336	-1.000
5	Retina	-12			
Optomechanical eye model					
1	Cornea	7.800	1.00	1.458	-0.50
2	Anterior chamber	6.700	4.45	1.334	0
3	Fused silica lens	11.462	3.70	1.458	0
4	Vitreous humor	-11.019	16.64	1.334	-3.25
5	Retina	-11			

sensor via an optical relay system. The human retina forms a curved image plane that naturally corrects the effect of field curvature, but existing eye models do not contain such capabilities. Therefore, none of the eye models accurately depicts the field of view and the true image quality. This deficiency seriously hinders the use of existing eye models in clinics or IOL development. The most salient feature of our eye model, aside from its realistic dimensions, is the custom optics at the retina position to map the curved image plane to a flat image plane compatible with the CMOS imager.

This article describes a life-size, cost-effective, and fluid-filled optomechanical eye model that can reliably reproduce the structures and functions of all image-forming components in the human eye, including the cornea, aqueous humor, crystalline lens, vitreous humor, and retina.

## MATERIALS AND METHODS

### LENS DESIGN

A fused silica lens-based system was used to make the equivalent of the crystalline lens and cornea in the human eye, with matching optical power. The crystalline lens in the human eye has a graded refractive index ranging from 1.38 to 1.40.<sup>13</sup> Reproducing such a graded index profile is technically challenging and would not provide significant improvements to the image resolution. Consequently, the silica lenses in the optomechanical eye model have a uniform index of refraction optimized for image quality along the optical axis. A set of optic components was then configured to match the on-axis characteristics of a specific human eye. Simulations and measurements were performed to ensure that the difference in the small-angle off-axis image quality between the specific human

eye and the modeled eye was minimal within the macular area. The optomechanical eye model was designed and constructed to allow all of the components to be replaced easily. In addition, the housing has the flexibility to accommodate varying dimensions, such as distances between any optical surfaces.

The design of the optomechanical eye model starts with ray-tracing simulations using ZEMAX software (Radiant Zemax, Redmond, WA). We used the widely accepted Navarro model to represent the human eye and found that the optimal parameters for the optomechanical eye model closely matched the image quality between our device and the Navarro human eye model.<sup>14</sup> **Table 1** shows the essential physical parameters of the Navarro model and the optomechanical eye model.

Our model uses fused silica optics with a refractive index of 1.458. We used a cornea lens that is 1 mm thick, with an anterior radius of 7.8 mm (conic constant:  $-0.5^{15}$ ) and a posterior radius of 6.7 mm. The greater thickness was chosen to improve the durability of the lens, and simulations indicated that this has a negligible effect on the resolution of the image. The fused silica lens that functions as the crystalline lens has an aspheric shape to minimize spherical aberration.

At the position of the retina we constructed a closely packed curved fiber bundle that matches the profile of the retina as the image surface. The curved fiber bundle consists of an array of optical fibers with a core diameter of 4  $\mu\text{m}$  and a center-to-center spacing of 4.2  $\mu\text{m}$ . The bundled fiber has an anterior radius of curvature of 11.019 mm to simulate the curvature of the retina and a flat posterior surface to allow image transformation onto a CMOS imager (6.4- $\mu\text{m}$  pixel size) with relay at optics with a magnification of  $2\times$ . The specially

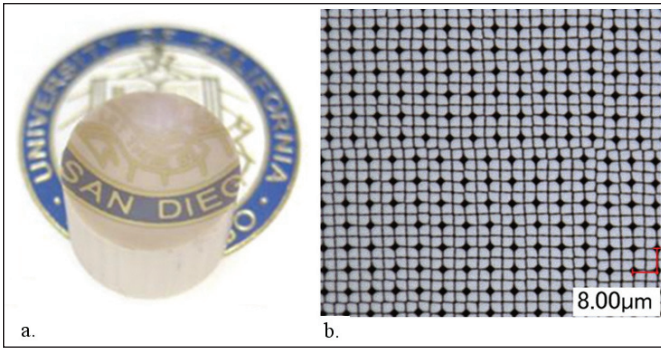


**Figure 1.** (A) Curved fiber bundle transmitting the University of California–San Diego emblem from the flat surface (bottom) to the curved surface (top). (B) Microscopic view of the fiber bundle. The white spots are the cores of the fibers and the black areas are insulating rods that prevent crosstalk between the fibers.

imager is beneath a protective glass cover, the light from the fiber bundle cannot be perfectly coupled to the image sensor. Consequently, we prefer to use an optical relay to transmit the image from the flat side to an imaging sensor. The material composition of the curved fiber bundle is proprietary; however, the refractive indices of the core and cladding are 1.820 and 1.485, respectively, producing a numerical aperture of 1.<sup>16</sup>

**OPTOMECHANICAL DESIGN**

For the mechanical design of the eye model, we machined the optomechanical housing of a 28-mm-diameter acetal resin (Delrin, DuPont, Wilmington, DE) sphere for the mechanical design of the optomechanical eye model. All of the optical components were mounted to the housing so that the spacing between any two elements may be adjusted to match the anatomy of individual patients’ eyes. We created an insert for the cornea and used ultraviolet curable epoxy to mount it to the housing as the first optical element to prevent water leakage. We threaded a 10-mm hole for inserting the pupil and the lens that simulates either the crystalline lens or the IOL. The lens is situated between a 1-mm-thick ring and a 3.75-mm-diameter pupil. The pupil size can be varied by simply substituting a ring with a different inner diameter. By measuring the focal distance of the microscope to the surface of each element during assembly, we ensured that all elements were aligned and correctly spaced to match the eye of interest. The errors in position of the optical elements depend on the accuracy of the microscope used for assembly and operation errors in adjusting the microscope focus. The latter is on the order of tens of microns. We then used a clamp to hold the curved fiber bundle as shown in **Figure 2B**. The clamp has three holes for springs and screws (M2 × 0.4) to allow ad-

designed fiber bundle was fabricated by Schott North America (Elmsford, NY). The integrated curved fiber bundle provides a field of view of 34.5 degrees, which is significantly larger than the field of view of the fovea in human eye, thus allowing us to evaluate the image quality both in the macular area and in the peripheral vision. The core-to-core spacing of 4.2 μm yields a spatial resolution of 128 cycles/mm that is comparable to the resolution of the macular area of the retina.

We treat each 4-μm diameter fiber as one pixel that carries light of all colors to the red, green, and blue pixels on the CMOS image. This closely resembles how light propagates within the eye and reaches the photoreceptors in the cones and rods on the retina. **Figure 1** shows the microscopic view of the bundled fiber. The white spots are the cores of the fibers, and the black areas are insulating rods that prevent crosstalk between the fibers. The image can be transmitted through the curved surface to the flat side of the fiber bundle and either detected directly or optically relayed to a CMOS imager. In practice, because the photosensitive area of a CMOS

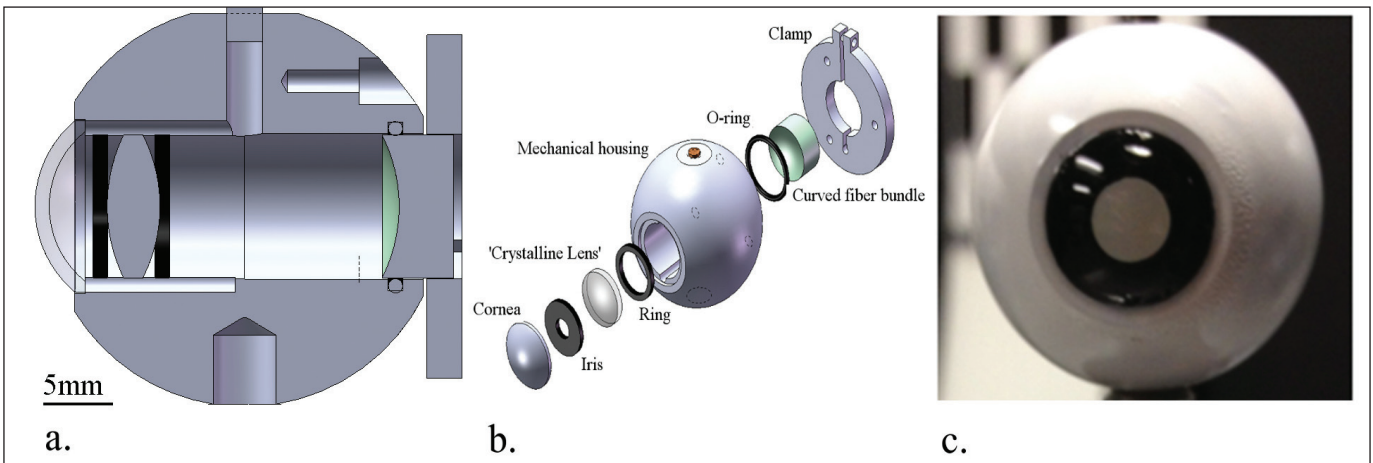


**Figure 2.** (A) Cross-sectional view of the optomechanical eye model. (B) Exploded view with the individual parts listed. (C) The assembled optomechanical eye model that is comparable to a life-size human eye.

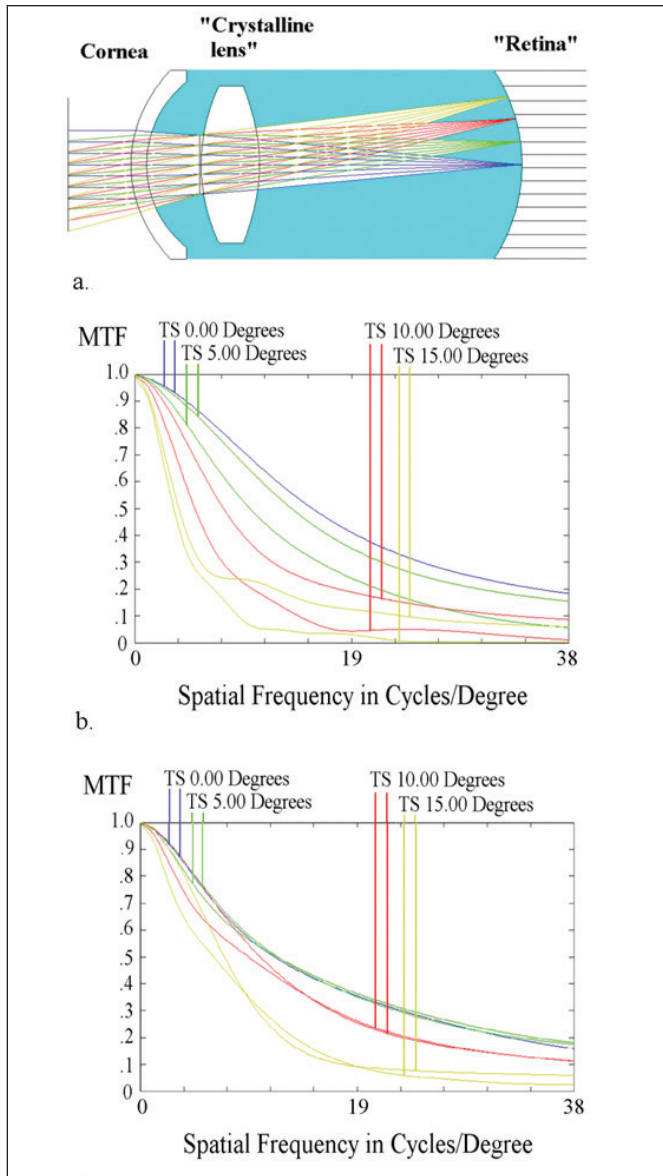


**Figure 3.** (A) Optical simulation of the optomechanical eye model using ZEMAX software (Radiant Zemax, Redmond, WA). (B and C) Polychromatic modulation transfer function (MTF) of the experimental optomechanical eye model and the Navarro eye, respectively, with a 4-mm pupil and an infinite object distance. The curves (T = tangential; S = sagittal) are colored and labeled according to the angles off the optical axis.

justment of the tilt and position. Each 90-degree rotation of a screw accounts for the fiber bundle to move along the direction of the channel. An O-ring in the back of the optomechanical eye model holds the curved fiber bundle in place and prevents water leakage (Figure 2). The threaded area also acts as baffles to limit the scatter of light off the walls. Channels were created on the top and bottom surfaces to act as an inlet and an outlet during water filling. The assembled optomechanical eye model was vacuum filled with distilled water with a refractive index of 1.334<sup>5,17</sup> to remove trapped gas

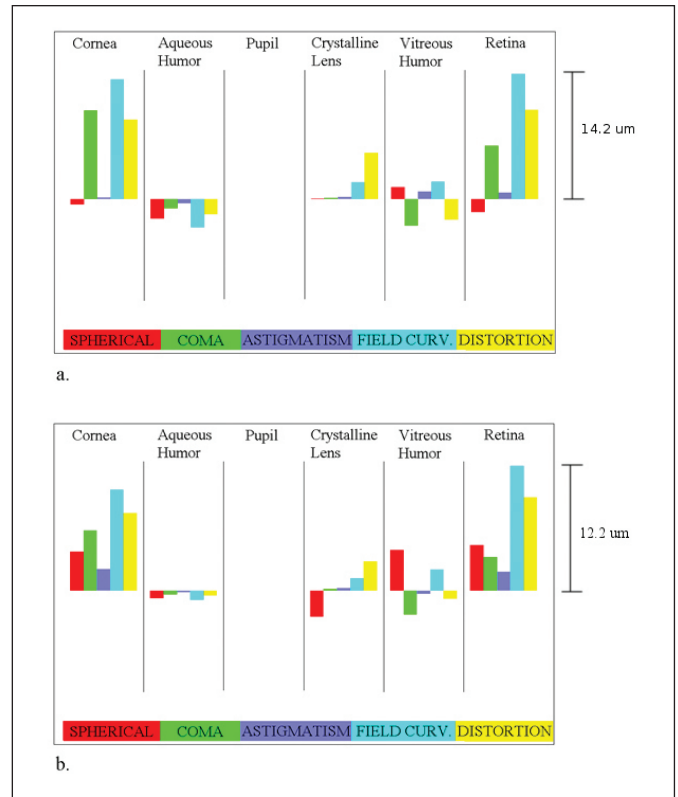


**Figure 4.** (A and B) Calculated Seidel aberration coefficients of each individual surface and their summation on the retina for the optomechanical eye model and the Navarro model, respectively. Both diagrams are calculated at a wavelength of 550 nm.

bubbles. Water was used as the medium because the index of water is very close (within 1%) to the index of aqueous humor and vitreous humor.

The optomechanical eye model was used to evaluate IOLs by characterizing two commercial AcrySoft IOLs (Alcon Laboratories, Fort Worth, TX): one diffractive IOL and one refractive IOL. Both IOLs have the same optical power of 16 diopters with an iris of approximately 3 mm. The IOLs were centered on a ring with the edges glued to the fixture. Their haptics were removed to fit the housing. Situated at the position of the crystalline lens in the optomechanical eye model, with the front surface of the IOL approximately 4 mm from the back surface of the cornea, preliminary results of the lenses were characterized with a modified 1951 U.S. Air Force resolution chart that was backlit by a halogen lamp for a qualitative comparison of the properties of two IOLs.

## RESULTS

### RAY-TRACING SIMULATION

ZEMAX software was used to simulate the resolution and quantify the aberrations of each optical component for the optomechanical eye model and the Navarro model (Figures 3 and 4). All simulations



**Figure 5.** Image of the stone bear on the University of California–San Diego campus. The object is approximately 25 m from the optomechanical eye model. The darkening around the edges is caused by the limitation of the numerical aperture of the fiber and its inability to couple light efficiently at high fields of view, similar to the Stiles-Crawford effect. The red circular area represents the equivalent of the macular region in the human eye.

were performed under polychromatic illumination with objects from an infinite distance and a pupil 3.75 mm in diameter. **Figure 3** shows that both the 0-degree and 5-degree off-axis images of the optomechanical eye model have similar resolution to that of the Navarro model. Both the Navarro model and the optomechanical eye model diminish in resolution with increasing field of view, but the resolution of the optomechanical eye model diminishes more quickly. Detailed analysis of optical aberrations, as shown in **Figure 4**, shows that the Navarro model has lower coma than the optomechanical eye model. On the other hand, the optomechanical eye model has less spherical aberration and astigmatism than the Navarro model. The distortion and field curvature are nearly identical in both models.

#### CHARACTERIZING THE OPTOMECHANICAL EYE MODEL

To characterize the optical properties of the optomechanical eye model, we measured the image sharpness of a slanted edge on a black and white chart, a standard technique for measuring the resolution of digital cameras. Using the optical assessment software, SFR Plus (Imatest, Boulder, CO) ([www.imatest.com/products/test-charts/sfr-plus-test-charts](http://www.imatest.com/products/test-charts/sfr-plus-test-charts)), we compared the modulation transfer function (MTF) produced by the optomechanical eye model at an infinite conjugate with the ZEMAX-simulated MTF. The results allow the quality of device fabrication and assembly to be assessed. Imatest measures sharpness by first obtaining the line spread function of image of a slanted edge and then con-

verting the line spread function into spatial frequency as a measure of the resolution of the device. This resolution is calculated in cycles or line-pairs per degree (cycles/degree or lp/degree). We adjusted the focal distance of the optomechanical eye model by moving the curved fiber bundle along the optical axis. To eliminate the constraints imposed by the mechanical assembly of commercial CMOS imagers, we used an optical relay system and a Canon EOS 5D Mark II camera (f-number, F/2.8; focal length, 100 mm; and exposure time, 0.3 seconds; Canon, Lake Success, NY) to capture the image projected on the surface of the curved fiber bundle. Because the relay optics transform the image from the flat, rear surface of the fiber bundle to another flat CMOS imager plane, this step introduces negligible artifacts to the image. Limited by the size (4  $\mu\text{m}$ ) of the individual fiber in the fiber bundle, the maximum achievable MTF is 38 cycles/degree. At 10% modulation depth, we obtained an on-axis resolution of approximately 34.0 and 33.1 cycles/degree for the horizontal and vertical MTFs, respectively. At 10 degrees off axis, the resolution is 7.8 and 8.8 cycles/degree for the horizontal and vertical MTFs, respectively (**Figure A**, available as supplemental material in the PDF version of this article). Although resolution targets provide quantitative assessments of the resolution of the model, images of normal objects obtained in daily life under daylight conditions provide more relevant information on the characteristics of the eye. **Figure 5** shows an image of the stone bear on the University of California–San Diego campus from a distance of approximately 25 m, obtained by the optomechanical eye model. The curved surface of the fiber bundle matches the curvature of the retina, but all of the fibers are packed in parallel with each other along the optical axis. When an image is formed on the curved surface and transmitted along the fiber, the image appears to be darker near the outer area.

#### INTRAOCULAR LENS TESTING

**Figures 6A and 6D** show images from both IOLs at an object distance of 15 feet. Then images were obtained at 3 feet (**Figures 6B and 6C**) and at 1 foot (**Figures 6E and 6F**) from the resolution chart. In **Figures 6A and 6D**, we cropped and digitally zoomed the center portion of the images without any other signal processing. The spatial frequency bars that can be resolved are shown in the figures.

#### DISCUSSION

Close examination of the Imatest results show that the on-axis values of the optomechanical eye model match the resolution of the healthy human eye, with a horizontal and vertical combined average of 33.5 cycles/

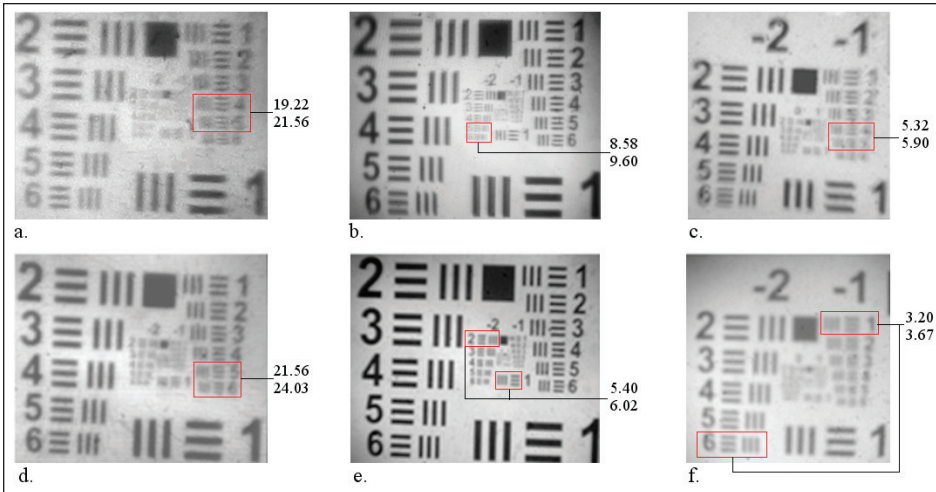


**Figure 6.** (A-C) Images of the 1951 U.S Air Force resolution chart taken by the optomechanical eye model with a diffractive intraocular lens (IOL) at distances of (A) 15 feet, (B) 3 feet, and (C) 1 foot. (D-F) The same images taken by the optomechanical eye model with a refractive IOL at distances of (D) 15 feet, (E) 3 feet, and (F) 1 foot. Digital zoom and cropping have been used to show the same features from images of different magnifications.

degree, better than 20/20 visual acuity. The resolution is still lower than the ZEMAX-simulated value. This may be attributed to the manufacturing tolerances and positions of the lenses and a possible tilt in the mounting of the curved fiber bundle. **Figure B** (available as supplemental material in the PDF version of this article) shows the Monte Carlo simulation using ZEMAX to show performance degradation as a result of manufacturing tolerances (thickness, radius, and astigmatism) and component misalignments within 0.1 mm and 1-degree tilt (2 degrees for the curved fiber bundle). As shown in **Figure B**, the experimental data for the on-axis resolution are significantly better than the calculated scenario, indicating that the manufacturing and assembly errors are lower than the magnitudes used in the simulation. Although the cornea of this model overcompensates for the spherical aberration compared with the Navarro model, the overall resolution of our eye model is significantly better than 20/20 visual acuity. Additionally, we can further reduce the tolerances on the tilt and decentration of the curved fiber bundle by using a clamp with a single-screw mechanism that would allow the fiber bundle to move easily along the optical axis.

The optomechanical eye model also experiences a darkening along the edges at the posterior side of the bundle. This is caused by the incident angles on the curved fiber bundle that refract and emit at larger angles with respect to the optical axis as the field of view increases (**Figure C**, available as supplemental material in the PDF version of this article). Because the optical relay has a limited numerical aperture, it cannot capture all of the light emitted from all of the fibers. The emission from the fiber bundle is not uniformly distributed across each of the solid angles, allowing for more light to be captured by the optical relay than was calculated. Using a tapered fiber bundle with all of the fibers oriented to be normal to the incident angles from any field of

view reduces the darkening affect along the edges. The light would be guided within the fiber with limited differences to the emitted solid angles from all of the fibers, producing a more uniform intensity profile.

Preliminary results with IOLs indicated that the multifocal IOL had a better depth of focus than the refractive IOL, as expected from the multifocal nature of the diffractive IOL. In our current optomechanical eye model, the achievable resolution of the IOL is generally lower than that of glass lenses because of difficulties in aligning the IOLs. The magnitudes of decentering and tilting errors are larger for IOLs because the area allotted for the IOL assembly is significantly greater than 0.1 mm, yielding a larger alignment error during assembly. This problem can be remedied in future optomechanical eye models by incorporating the haptics into the optomechanical design and creating a more accurate mounting fixture.

We demonstrated a life-size optomechanical eye model that can produce resolution similar to the raw images projected onto the human retina. The optomechanical design of the eye model can be easily customized to model the eyes of individual patients, thus allowing ophthalmologists to visualize the unprocessed images produced by different combinations of lenses and visual effects. The optomechanical model eye can also find applications in other optical instruments for vision inspection and research.

**AUTHOR CONTRIBUTIONS**

*Study concept and design (AA, JEF, YL, EJT); data collection (AA, IS); analysis and interpretation of data (AA); drafting of the manuscript (AA, YL); critical revision of the manuscript (AA, YL, DJS, EJT, IS); supervision (DJS)*

**REFERENCES**

1. Alió JL, Ben-Nun J, Rodríguez-Prats JL, Plaza AB. Visual and accommodative outcomes 1 year after implantation of an accom-

- modating intraocular lens based on a new concept. *J Cataract Refract Surg.* 2009;35(10):1671-1678.
2. Kelly SP, Jalil A. Wrong intraocular lens implant: learning from reported patient safety incidents. *Eye (Lond).* 2009;25(6):730-734.
  3. Piers PA, Manzanera S, Prieto PM, Gorceix N, Artal P. Use of adaptive optics to determine the optimal ocular spherical aberration. *J Cataract Refract Surg.* 2007;33(10):1721-1726.
  4. Artal P, Manzanera S, Piers P, Weeber H. Visual effect of the combined correction of spherical and longitudinal chromatic aberrations. *Opt Express.* 2010;18(2):1637-1648.
  5. Gobbi PG, Fasce F, Bozza S, Brancato R. Optomechanical eye model with imaging capabilities for objective evaluation of intraocular lenses. *J Cataract Refract Surg.* 2006;32(4):643-651.
  6. Gobbi PG, Carones F, Brancato R. Optical eye model for photorefractive surgery evaluation. *Proc SPIE.* 1999;3591:10-21.
  7. Barcik A, Nowak J, Siedlecki D, Zajac M, Zarówny J. Physical model of human eye with implantable intraocular lenses. *Proc SPIE.* 2008;7141(71411A):1-8.
  8. Piers P, Sverker Norrby N, Mester U. Eye models for the prediction of contrast vision in patients with new intraocular lens designs. *Opt Lett.* 2004;29(7):733-735.
  9. Terwee T, Weeber H, van der Mooren M, Piers P. Wavefront measurements of diffractive and refractive multifocal intraocular lenses in an artificial eye. *J Refract Surg.* 2008;24(3):308-311.
  10. Norrby S, Piers P, Campbell C, van der Mooren M. Model eyes for evaluation of intraocular lenses. *Appl Opt.* 2007;46(26):6595-6605.
  11. Campbell CE. Wavefront measurement of diffractive and refractive multifocal intraocular lenses in an artificial eye. *J Refract Surg.* 2008;24(3):308-311.
  12. Bakaraju RC, Ehrmann K, Falk D, Ho A, Papas E. Physical human model eye and methods of its use to analyze optical performance of soft contact lenses. *Opt Express.* 2010;18(16):16868-16882.
  13. Liou H, Brennan N. Anatomically accurate, finite model eye for optical modeling. *J Opt Soc Am A.* 1997;14(8):1684-1695.
  14. Navarro R, Santamaría J, Bescós J. Accommodation-dependent model of the human eye with aspherics. *J Opt Soc Am A.* 1985;2:1273-1281.
  15. Atchison D, Smith G. *Optics of the Human Eye.* Edinburgh: Butterworth-Heinemann; 2000.
  16. Hancock JJ. The design, fabrication, and calibration of a fiber filter spectrometer. Doctoral dissertation. University of Arizona, Tucson, 2012.
  17. Pieh S, Marvan P, Lackner B, et al. Quantitative performance of bifocal and multifocal intraocular lenses in a model eye: point spread function in multifocal intraocular lenses. *Arch Ophthalmol.* 2002;120(1):23-28.

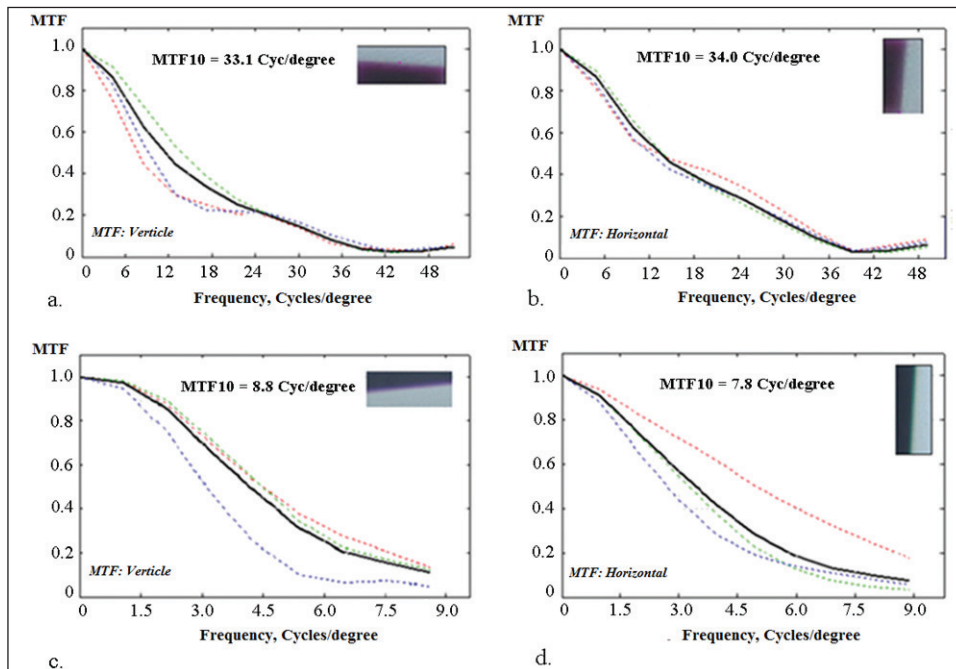


**Figure A.** (A and B) On-axis polychromatic modulation transfer function (MTF) measured from the optomechanical eye model using a slanted edge chart. (C and D) Ten degrees off-axis MTF measured from the eye model using the slanted edge chart. Images are illuminated with fluorescent lighting. The images of the slanted edge chart are shown in the insets.

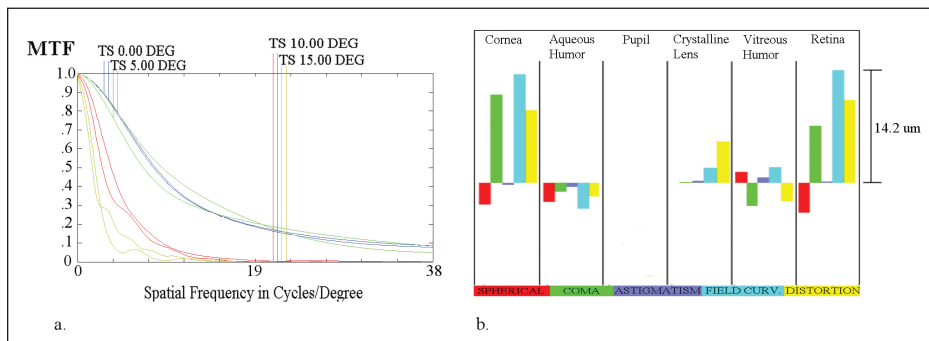


**Figure B.** (A) Potential scenario of loss of resolution because of manufacturing and assembly tolerances. (B) Potential scenario of calculated Seidel aberration coefficients from manufacturing and assembly tolerances. MTF = modulation transfer function; S = sagittal; T = tangential.

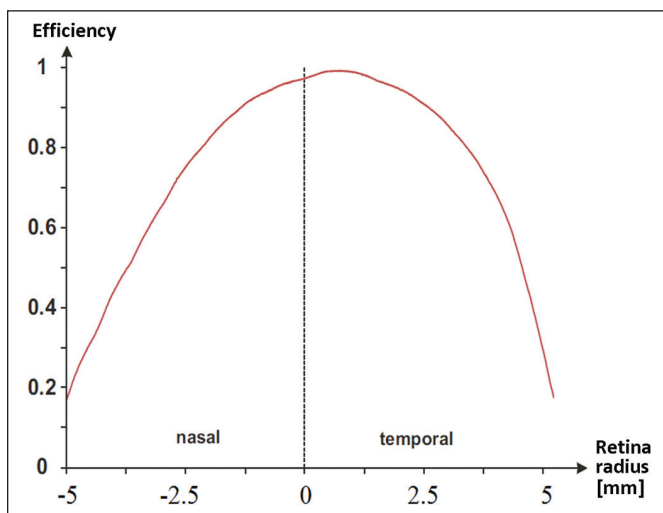


**Figure C.** Relative intensity distribution across the fiber bundle along its vertical axis. The screen was uniformly illuminated at an angle with respect to the optomechanical eye model, causing the tilt in the relative intensity plot.